Highly stable and differentially arranged hexanuclear lanthanide clusters: structure, assembly mechanism, and magnetic resonance imaging†

Wen-Wen Qin,[a] Yun-Lan Li,[a] Zhong-Hong Zhu, [ID] *[a] Fu-Pei Liang,[a] Qiong Hu*[b] and Hua-Hong Zou [ID] *[a]

The directed and controllable synthesis of lanthanide clusters with precise structures has received considerable research attention, however, progress in such remains sluggish. The steps performed in a reaction system under "black-box" conditions are unpredictable and have very low controllability. The precise customization of lanthanide clusters with the same number of cores but different arrangements is particularly difficult. Using bis-acylhydrazone-derived multidentate chelating ligands with different substituents, differentially arranged hexanuclear lanthanide clusters (**Dy₆** and **HNP-Dy₆**) with identical core connections but different template-motif arrangements were constructed herein for the first time using a multidentate chelating coordination method. Specifically, **Dy₆** with face-to-face and dislocation-arrangement template motifs was obtained using $-N(Et)_2$-substituted bis-acylhydrazone ligands with a strong steric hindrance effect. Changing $-N(Et)_2$ to a benzene ring with a strong $\pi-\pi$ interaction yielded **HNP-Dy₆** with inverted and coplanar arrangements of template motifs. The controllable construction of these two hexanuclear dysprosium clusters represented great progress in the precise synthesis of lanthanide clusters. High-resolution electrospray ionization–mass spectrometry (HRESI–MS) with different ion-source energies demonstrated the high stabilities of **Dy₆** and **HNP-Dy₆** in solutions. Time-dependent HRESI–MS tracked the formation processes of **Dy₆** and **HNP-Dy₆** and led to the following possible self-assembly mechanisms: $L^1 + 2Dy \rightarrow Dy_2L^1 \rightarrow Dy_3L^1 \rightarrow Dy_6(L^1)_2$ and $L^2 + 2Dy \rightarrow Dy_2L^2 \rightarrow Dy_3L^2 \rightarrow Dy_5(L^2)_2/Dy_6(L^2)_2 \rightarrow Dy_6(L^2)_2$. At 1-T magnetic field, the longitudinal and transverse relaxation rates of **Gd₆** were 12.06 and 24.10 mM^{-1} s^{-1}, respectively. **Gd₆** with highly aggregated Gd(III) exhibited high relaxation rates, indicating its great potential as a T_1-weighted magnetic resonance imaging contrast agent. This work provides an example of the design and synthesis of lanthanide clusters with high stabilities and relaxation rates, taking a big step toward the precise and controllable synthesis of lanthanide clusters.

Introduction

Lanthanide clusters with a precise structure, a uniform nanoscale size, and rich functions have attracted widespread attention and have shown great application prospects in the fields of molecular magnetism, magnetocaloric effect, bio-imaging,

[a]School of Chemistry and Pharmaceutical Sciences, State Key Laboratory for Chemistry and Molecular Engineering of Medicinal Resources, Guangxi Normal University, Guilin 541004, P. R. China. E-mail: 18317725515@163.com, gxnuchem@foxmail.com

[b]Guangxi Key Laboratory of Agricultural Resources Chemistry and Biotechnology, College of Chemistry and Food Science, Yulin Normal University, Yulin 537000, P. R. China. E-mail: huqiongscut@163.com
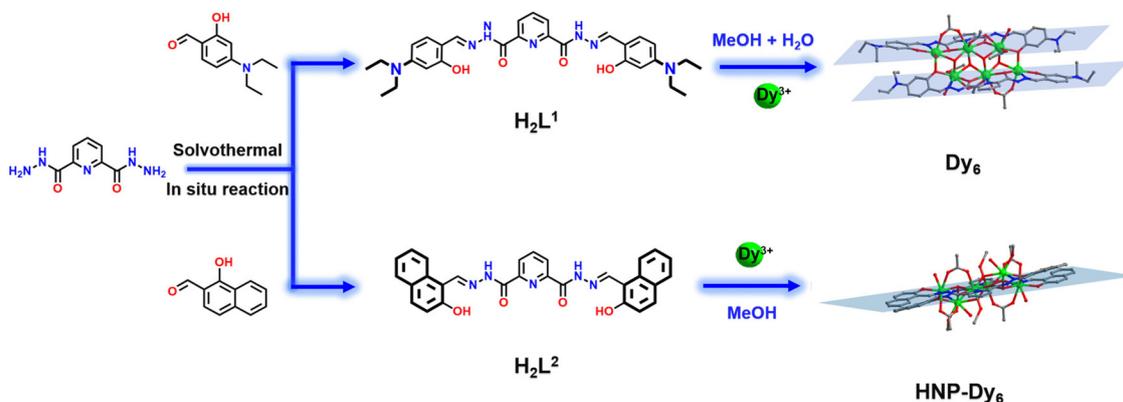
solid-state luminescence, *etc*.[1–11] In particular, gadolinium(III) clusters with a nanometer size and highly concentrated metal centers break through the limitations of conventional magnetic resonance imaging (MRI) contrast agents (CAs) and exhibit a high imaging contrast.[12,13] According to the Solomon–Bloembergen Morgan (SBM) paramagnetic relaxation theory, it can be known that CAs with high relaxation, high resolution and high contrast can be obtained by connecting multiple single-nuclear or low-nuclear gadolinium complexes through multi-component integration. High-nuclear gadolinium clusters with highly aggregated Gd(III) undoubtedly show attractive application prospects in the field of MRI. In 2020, Sun *et al.* used 2,6-pyridine bistetrazolium-derived ligands with different bending angles to construct a water-soluble molecular cage Ln$_{2n}$L$_{3n}$, which showed high relaxation rates and excellent *in vivo* MRI imaging effects in mice.[13] In

This journal is © the Partner Organisations 2023

Inorg. Chem. Front., 2023, **10**, 6269–6281 | **6269**

2023, Tong *et al.* used solvothermal synthesis technology to construct spherical nanoclusters Gd_{32} with high stability, low toxicity and excellent water solubility. The highly aggregated Gd(III) in the structure leads to its excellent MRI imaging contrast both *in vivo* and *in vitro*.[12] Although substantial progress has been made in the application and expansion of lanthanide clusters, progress with regard to their controllable and precise synthesis remains unsatisfactory.[14] Previously, lanthanide clusters primarily relied on hydrolysis and the anion template method to guide their structural synthesis. Various lanthanide clusters with beautiful shapes and diverse topologies, such as wheel-shaped Gd_{140}, caged Gd_{60}, hamburger-shaped Dy_{76}, and tubular Dy_{72}, have been constructed based on the abovementioned methods.[15–19] In 2018, Bu *et al.* induced the synthesis of a rare hamburger-shaped dysprosium cluster Dy_{76} using a mixed-anion template that can be regarded as an assembly of two Dy_{48} clusters. In 2016, Zheng *et al.* synthesized a tubular dysprosium cluster Dy_{72} by controlling the hydrolysis of Dy(III) ions with *N*-methyldiethanolamine.[19] In 2022, Zheng *et al.* synthesized multinuclear lanthanide hydroxide clusters under the guidance of combined I^- and CO_3^{2-} as mixed templates.[20] The complex reaction and the extremely low controllability of the reaction system that lead to directional construction of lanthanide clusters remain to be very vague.
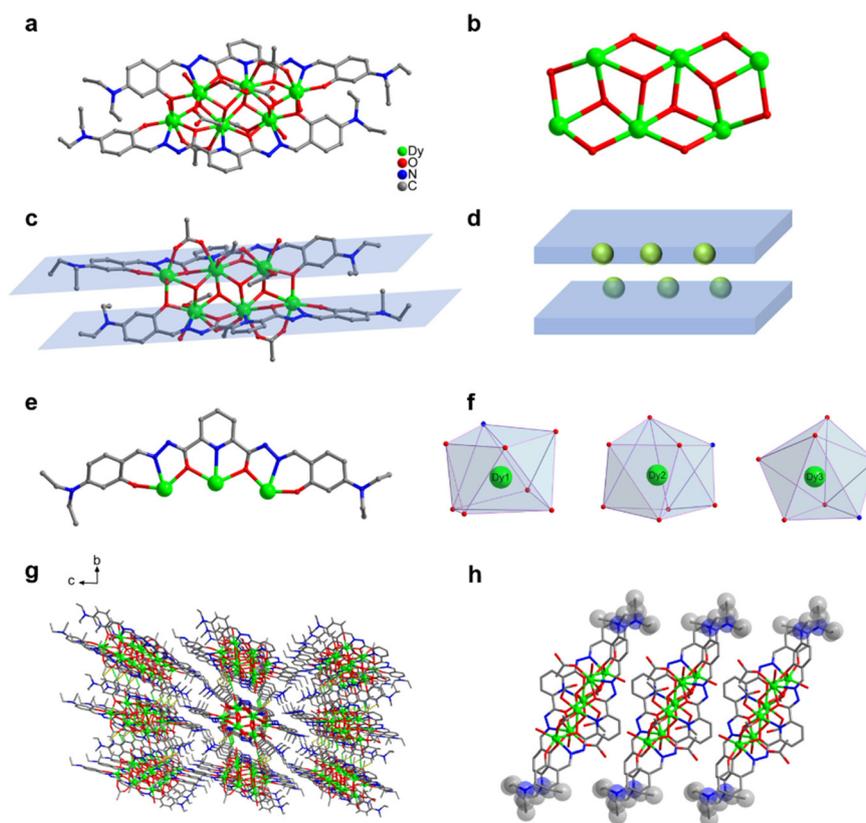
The tracking of the self-assembly process and the study of the self-assembly mechanism have accelerated the pace of the directional and rational construction of lanthanide clusters.[21–23] Since 2018, we have been using crystallography combined with high-resolution electrospray ionization–mass spectrometry (HRESI-MS) to explore and analyze the formation process and the self-assembly mechanism of several lanthanide clusters. We also proposed the out-to-in, linear, and annular growth mechanisms to guide the directional synthesis of lanthanide clusters.[24–28] In 2020, our research group successfully constructed a double-cage dysprosium cluster Dy_{60} using a multidentate chelating coordination method, tracked the Dy_{60} formation process using HRESI-MS, and proposed the possible self-assembly mechanism of Dy_{60}.[29] In 2021, we first proposed that the out-to-in growth mechanism guides the

directional construction of 16 nuclear discotic lanthanide clusters.[25,26,30] In 2022, also for the first time, we guided the directional construction of chiral lanthanide clusters with different connection modes and shapes by manipulating the annular growth mechanism.[27] We then successfully constructed the largest planar disk-shaped lanthanide cluster Dy_{19} under solvothermal conditions and proposed its possible assembly mechanism (*i.e.*, the planar epitaxial or planar internal growth mechanism).[31] The bulky bis-acylhydrazone and Schiff base-derived ligands with multidentate chelation coordination sites can quickly capture the lanthanide metal ions in solutions to form template units, thereby further assembling to obtain the target lanthanide clusters.[24,32,33] These template units formed by linking lanthanide ions with bulky chelating ligands have a higher stability in solution than hydrolyzed products and anion templates, making the self-assembly process of lanthanide clusters more regular and promoting their designability.[14] Based on the abovementioned foundations, we focus herein on the precise construction of lanthanide clusters with the same core connections but different template-motif arrangements, which has been difficult to achieve until now.

In this work, we use the $-N(Et)_2$-substituted bis-acyl-hydrazone-derived ligand H_2L_1 (N'^2,N'^6-bis(4-(diethylamino)-2-hydroxybenzylidene)pyridine-2,6-dicarbohydrazide) and $Dy(OAc)_3 \cdot 4H_2O$ to perform a reaction under solvothermal conditions and acquire a **Dy$_6$** sample, which has face-to-face and dislocation-arrangement template motifs (Scheme 1). Changing $-N(Et)_2$ to a benzene ring with a strong π–π interaction yields **HNP-Dy$_6$** with an inverted and coplanar arrangement of template motifs (Scheme 1). We employ HRESI-MS to evaluate the stabilities of the two hexanuclear clusters prepared in this study in a solution. Under the condition of an increasing ion-source energy from 0 to 100 eV, the molecular-ion peaks of **Dy$_6$** and **HNP-Dy$_6$** in the solution are found to be related to their structural skeletons, indicating that they both maintain a high stability in the solution. We implement time-dependent HRESI-MS to track the species changes during the **Dy$_6$** and **HNP-Dy$_6$** formations under solvothermal "black-box"

Scheme 1 Schematic of the **Dy$_6$** and **HNP-Dy$_6$** synthesis.

6270 | *Inorg. Chem. Front.*, 2023, **10**, 6269–6281

This journal is © the Partner Organisations 2023

Fig. 1 (a) Dy_6 structure, (b) cluster core connection, (c) face-to-face and up-and-down dislocation arrangements of the $Dy_3(L^1)$ template units, (d) schematic of the template-unit arrangement in Dy_6, (e) coordination mode of ligand $(L^1)^{2-}$, (f) coordination configurations of the metal-centered ions Dy_1-Dy_3 (g) three-dimensional Dy_6 accumulation, and (h) arrangement among the three independent units of Dy_6.

reaction conditions. The intermediates of various reactions are identified. Their possible self-assembly mechanisms are proposed as follows: $L^1 + 2Dy \rightarrow Dy_2L^1 \rightarrow Dy_3L^1 \rightarrow Dy_6(L^1)_2$ and $L^2 + 2Dy \rightarrow Dy_2L^2 \rightarrow Dy_3L^2 \rightarrow Dy_5(L^2)_2/Dy_6(L^2)_2 \rightarrow Dy_6(L^2)_2$. To the best of our knowledge, this is the first time that multidentate chelation coordination is manipulated through substitution effects to construct heterogeneous hexanuclear lanthanide clusters with the same cluster core connections but different template-motif arrangements. The high cluster stability in the solution promotes the expansion of its application in the solution. Notably, low Gd_6 concentration exhibits high longitudinal and transverse relaxation rates (r_1 and r_2, respectively) at 1-T magnetic field, indicating its great potential as a T_1-weighted MRI CA. This work paves a way for the directed and controllable synthesis of lanthanide clusters with precise structures and promotes the progress of lanthanide-cluster crystal engineering.

Results and discussion

Synthesis and structural analysis of Ln_6 clusters (Ln = Dy and Gd)

Approximately 0.4 mmol of $Dy(OAc)_3 \cdot 4H_2O$ and 0.05 mmol of the organic ligand H_2L^1 (N'^2,N'^6-bis(4-(diethylamino)-2-hydroxybenzylidene)pyridine-2,6-dicarbohydrazide) were accurately

weighed and dissolved in a mixed solvent of $MeOH : H_2O$ (1.0 mL : 0.3 mL) and added with 100 μL of triethylamine. After an even mixing, the reaction was derived under solvothermal conditions at 80 °C for 48 h to obtain an orange blocky crystal of Dy_6 (Fig. 1). The results of single-crystal X-ray diffraction (SCXRD) showed that Dy_6 crystallized in the $P\bar{1}$ space group of the triclinic system (Tables S1–S4†). Dy_6 comprised six Dy(III) ions, two multidentate chelating ligands $(L^1)^{2-}$, four $\mu_3\text{-}O^{2-}$, six OAc^-, and four terminally coordinated H_2O molecules and had the following molecular formula: $[Dy_6(L^1)_2(\mu_3\text{-}O)_4(OAc)_6(H_2O)_4]$ (Fig. 1a). The six metal-centered Dy(III) ions of Dy_6 were distributed on the equatorial plane and connected by oxygen atoms in the ligands and $\mu_3\text{-}O^{2-}$ bridges to form the {Dy/O} cluster nucleus (Fig. 1b). The multidentate chelating ligand $(L^1)^{2-}$ chelated three Dy(III) ions to form the $Dy_3(L^1)$ template motif. Notably, in the Dy_6 structure, two $Dy_3(L^1)$ were arranged in face-to-face and up-and-down dislocation arrangements (Fig. 1c and d, respectively). The two ligands at the cluster core periphery tightly wrapped the cluster core to resist the attack of foreign solvent molecules, further ensuring the Dy_6 stability. Each ligand chelated three Dy(III) ions and had the following coordination modes: $\mu_3\text{-}\eta^1:\eta^1:\eta^2:\eta^1:\eta^2:\eta^1:\eta^1$ (Fig. 1e). The six metal-centered Dy(III) ions in the Dy_6 structure had three coordination environments. The metal-centered Dy1 had an O_7N coordination

This journal is © the Partner Organisations 2023

Inorg. Chem. Front., 2023, **10**, 6269–6281 | **6271**

environment provided by the $(L^1)^{2-}$ ligand, μ_3-O^{2-}, OAc^-, and H_2O molecule (Fig. 1f). The SHAPE calculations showed that the coordination configuration was a Johnson biaugmented trigonal prism (J50) with a C_{2v} symmetric environment (Table S4†). The metal-centered Dy2 had an O_7N coordination environment provided by the $(L^1)^{2-}$ ligand, μ_3-O^{2-}, and OAc^- (Fig. 1f). The SHAPE calculations demonstrated that the coordination configuration was a biaugmented trigonal prism (J50) with a C_{2v} symmetric environment (Table S4†). Meanwhile, the metal-centered Dy3 had an O_6N_2 coordination environment provided by the $(L^1)^{2-}$ ligand, μ_3-O^{2-}, OAc^-, and H_2O molecule (Fig. 1f). The SHAPE calculations for this indicated that the coordination configuration was a Johnson pentagonal bipyramid (J13) with a D_{5h} symmetric environment (Table S4†). According to further weak interaction analysis and stacking diagrams, the strong steric hindrance of $-N(Et)_2$ caused the template units in the **Dy₆** structure to form face-to-face and dislocation arrangements (Fig. 1g and f). The structural analysis demonstrated that all the Dy–O/N bond lengths were within the normal range (Table S2†). We changed the metal salt to $Gd(OAc)_3 \cdot H_2O$ and obtained the **Gd₆** homologue of **Dy₆** under the same conditions.
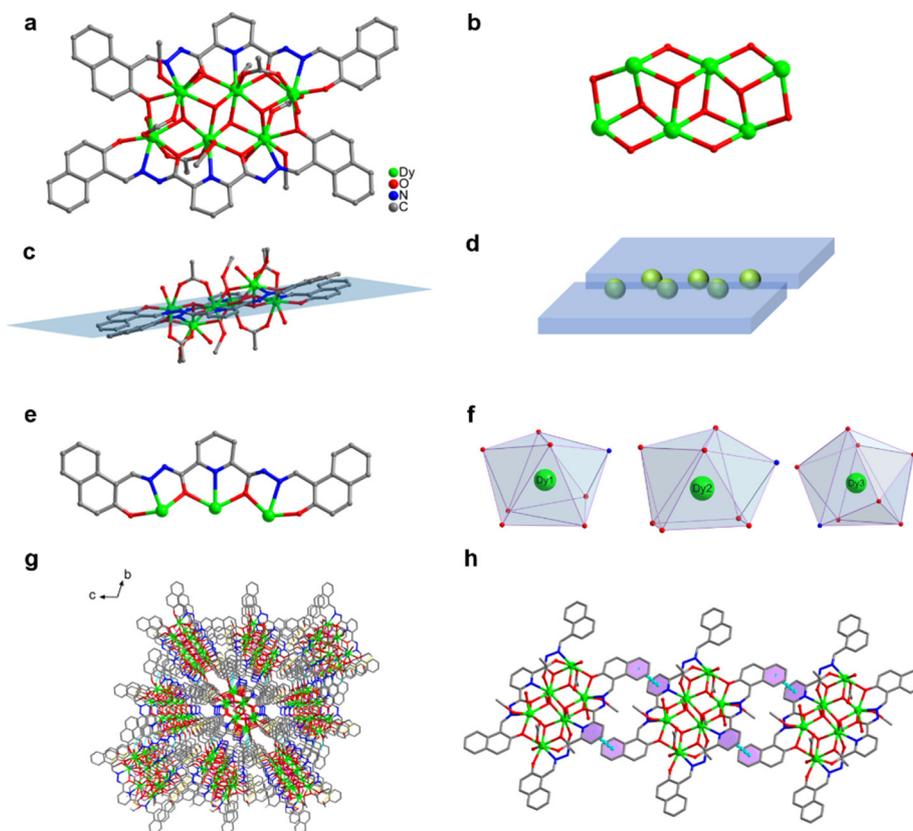
We changed 4-(diethylamino)salicylaldehyde to 2-hydroxy-1-naphthaldehyde to construct a diacylhydrazone-derived ligand, H_2L^2 (N'^2,N'^6-bis((2-hydroxynaphthalen-1-yl)methylene)pyridine-2,6-dicarbohydrazide). The yellow blocky crystals of **HNP-Dy₆** in Scheme 1 were obtained when the abovementioned solvothermal reaction was realized using H_2L^2 and the solvent was changed to 2.0 mL of anhydrous methanol. The SCXRD results showed that **HNP-Dy₆** crystallized in the $P\bar{1}$ space group of the triclinic system (Tables S1–S4†). **HNP-Dy₆** comprised six Dy(III) ions, two multidentate chelating ligands $(L^2)^{2-}$, four μ_3-O^{2-}, four OAc^-, four CH_3O^-, and four terminally coordinated H_2O molecules with the following molecular formula: $[Dy_6(L^2)_2(\mu_3\text{-}O)_4(OAc)_4(CH_3O)_4(H_2O)_4] \cdot 3CH_3OH$ (Fig. 2a). Similarly, the six metal-centered Dy(III) ions in the **HNP-Dy₆** structure were also distributed on the equatorial plane and connected by oxygen atoms in the ligands and μ_3-O^{2-} bridges to form the {Dy/O} cluster nucleus (Fig. 2b). The **HNP-Dy₆** structure comprised a multidentate chelating ligand that chelated three Dy(III) ions to form the $Dy_3(L^2)$ template unit. Surprisingly, the two $Dy_3(L^2)$ template units were found in the same plane and arranged in face-to-face and parallel arrangements, which was considerably different from **Dy₆** (Fig. 2c and d). The coordination mode of the multidentate chelating ligand $(L^2)^{2-}$ was μ_3-$\eta^1{:}\eta^1{:}\eta^2{:}\eta^1{:}\eta^2{:}\eta^1{:}\eta^1$ (Fig. 2e). The six metal-centered Dy(III) ions in the **HNP-Dy₆** structure all had an O_7N coordination environment. Their coordination configurations were Johnson biaugmented trigonal prism (J50) (Dy1), biaugmented trigonal prism (Dy2), and triangular dodecahedron (Dy3) (Fig. 1f and Table S5†). An obvious π–π stacking (3.820 Å) was observed in the **HNP-Dy₆** structure. The strong π–π interaction led to the reverse and planar arrangement of the template units (Fig. 2g and h). The structural analysis demonstrated that all the Dy–O/N bond lengths were within the normal range (Table S3†).

The controllable construction of the two distinct hexanuclear dysprosium clusters marked a great progress in the precise lanthanide-cluster synthesis. We initially proposed the multidentate chelating coordination (MCC) method for the rational construction of lanthanide clusters. For the first time, we selected herein a diacylhydrazone-derived ligand with multiple coordination sites and manipulated the MCC method to realize the precise synthesis of planar and dislocation-parallel differential hexanuclear dysprosium clusters. Specifically, when the substituent $-N(Et)_2$ with a large steric hindrance was selected, **Dy₆** was obtained with template units having face-to-face and upper and lower dislocation arrangements. Further increasing the conjugated ring on the ligand yielded **HNP-Dy₆** with template units located in the same plane and arranged face-to-face. To the best of our knowledge, most of the reported hexanuclear lanthanide clusters tend to be in the second arrangement. Precisely controlling and obtaining lanthanide clusters with the same cluster nuclei but different arrangements is difficult. Adjusting the multidentate chelating-ligand substituents enabled us to realize the directional assembly of heterogeneous hexanuclear lanthanide clusters with different arrangements. We were also able to reveal the controllability of the structural design of the hypernuclear lanthanide clusters, which is a big step toward a precise synthesis.

The thermal stability analysis of **Dy₆** and **HNP-Dy₆** was performed under a flowing N_2 atmosphere. The temperature was slowly increased from 35 °C to 1000 °C at a 5 °C min^{-1} rate (Fig. S2†). As the temperature was gradually increased from 35 °C to 140 °C, we obtained a **Dy₆** weight loss rate of 5.18% that corresponded to the loss of four terminally coordinated water molecules and one OAc^-. The theoretical value for this was 5.13%. The **Dy₆** weight loss rate was 11.60% when the temperature was increased from 310 °C to 405 °C. This process corresponded to the loss of five OAc^-. The theoretical value for this was 11.55%. Finally, **Dy₆** was rapidly decomposed at a temperature above 480 °C (Fig. S2a†). Similarly, the **HNP-Dy₆** weight loss rate was 6.53% when the temperature was gradually increased from 35 °C to 115 °C. This corresponded to the loss of four terminally coordinated water molecules and three methanol molecules. The theoretical value for this was 6.78%. The **HNP-Dy₆** weight loss rate was 11.14% when the temperature was gradually increased from 32 °C to 390 °C. This rate corresponded to the loss of four terminally coordinated CH_3O^- and three OAc^-. The theoretical value for this was 11.70%. Finally, the **HNP-Dy₆** structure was rapidly decomposed at a temperature of >500 °C (Fig. S2b†). The powder X-ray diffraction experimental and simulated values for **Dy₆**, **Gd₆**, and **HNP-Dy₆** were compared at 35 °C. The results showed their pure phases (Fig. S3†).

Stabilities of Dy₆ and HNP-Dy₆

In recent years, HRESI-MS had been extensively used to evaluate the stability, solubility, and ionization degree of the lanthanide clusters in solutions.[6,12,29,34] In this work, to further explore the stabilities of **Dy₆** and **HNP-Dy₆** in solution, we used HRESI-MS with different ion-source energies to monitor the

6272 | *Inorg. Chem. Front.*, 2023, **10**, 6269–6281

This journal is © the Partner Organisations 2023

Fig. 2 (a) **HNP-Dy$_6$** structure, (b) cluster core connection, (c) face-to-face arrangement of the Dy$_3$(L^2) template units in the same plane, (d) schematic of the template-unit arrangement in **HNP-Dy$_6$**, (e) ligand coordination mode, (f) metal-centered coordination configuration, (g) three-dimensional **HNP-Dy$_6$** accumulation, and (h) π−π stacking of the three independent units of **HNP-Dy$_6$**.

molecular-ion peak fragments of **Dy$_6$** and **HNP-Dy$_6$**. We specifically dissolved small amounts of pure **Dy$_6$** and **HNP-Dy$_6$** in chromatographic *N,N*-dimethylformamide (DMF) and performed HRESI-MS testing after extensive dilution using chromatographic methanol. The yielded data were collected within the *m/z* = 400–4000 range (Fig. 3a and 4a and Tables S6 and S7†). The results showed that **Dy$_6$** can maintain a high stability under the HRESI-MS conditions. The captured molecular-ion peaks of different *m/z* were related to the structural framework that can be assigned to $[Dy_6(L^1)_2(O)_4(CH_3COO)_x(OH)(solv.)]$ ($x \leq 5$; solv. = DMF, CH$_3$OH, and H$_2$O; +1, +2 valence). The abovementioned molecular-ion peak fragments were specifically resolved as $[Dy_6(L^1)_2(O)_4(OH)_4(CH_3OH)_3(H_2O)_2]^{2+}$ (calc. 1163.59, exp. 1163.54), $[Dy_6(L^1)_2(O)_4(CH_3COO)_2(OH)_2(CH_3OH)_2]^{2+}$ (calc. 1172.58, exp. 1172.55), $[Dy_6(L^1)_2(O)_4(CH_3COO)_2(OH)_2(CH_3OH)_2(H_2O)]^{2+}$ (calc. 1181.09, exp. 1181.08), $[Dy_6(L^1)_2(O)_4(OH)_4(DMF)_2(CH_3OH)]^{2+}$ (calc. 1188.10, exp. 1188.08), $[Dy_6(L^1)_2(O)_4(CH_3COO)_4(OH)(H_2O)_3]^+$ (calc. 2435.17, exp. 2435.16), $[Dy_6(L^1)_2(O)_4(CH_3COO)_5(DMF)(H_2O)]^+$ (calc. 2513.20, exp. 2513.18), and $[Dy_6(L^1)_2(O)_4(CH_3COO)_4(OH)(DMF)(CH_3OH)_2(H_2O)_3]^+$ (calc. 2572.26, exp. 2572.22) (Fig. S4 and Table S6†). Similarly, **HNP-Dy$_6$** presented a +1 valent molecular-ion peak fragment related to the structural framework in the *m/z* = 2000–3000 range, which can be attributed to $[Dy_6(L^2)_2(O)_4(CH_3COO)_x(CH_3O)_y$

(solv.)] ($x \leq 4$; $y \leq 4$; solv. = DMF, CH$_3$OH, and H$_2$O). The molecular-ion peak fragments were assigned to $[Dy_6(L^2)_2(O)_4(CH_3COO)_2(CH_3O)(OH)_2(H_2O)_2]^+$ (calc. 2261.91, exp. 2261.87), $[Dy_6(L^2)_2(O)_4(CH_3COO)_2(CH_3O)_3(CH_3OH)(H_2O)]^+$ (calc. 2302.96, exp. 2302.89), $[Dy_6(L^2)_2(O)_4(CH_3COO)_2(CH_3O)_3(CH_3OH)(H_2O)_2]^+$ (calc. 2321.97, exp. 2321.89), $[Dy_6(L^2)_2(O)_4(CH_3COO)_4(CH_3O)(CH_3OH)(H_2O)_2]^+$ (calc. 2375.96, exp. 2375.94), $[Dy_6(L^2)_2(O)_4(CH_3COO)_4(CH_3O)(CH_3OH)_5(H_2O)_5]^+$ (calc. 2560.09, exp. 2560.02), and $[Dy_6(L^2)_2(O)_4(CH_3COO)_4(CH_3O)(CH_3OH)_5(H_2O)_6]^+$ (calc. 2576.10, exp. 2576.04) (Fig. S5 and Table S7†).

Only the molecular-ion peaks $[Dy_6(L^1)_2(O)_4(OH)_4(CH_3OH)_3(H_2O)_2]^{2+}$ (calc. 1163.59, exp. 1163.56) and $[Dy_6(L^1)_2(O)_4(CH_3COO)_4(OH)(H_2O)_3]^+$ (calc. 2435.16, exp. 2435.17), which were related to the complete structural skeleton, were detected in the **Dy$_6$** solution as the ion-source voltage was gradually increased from 0 to 100 eV (Fig. S6 and Table S8†). **HNP-Dy$_6$** also only depicted the molecular-ion peak fragment of $[Dy_6(L^2)_2(O)_4(CH_3COO)_4(CH_3O)(CH_3OH)_5(H_2O)_5]^+$ (calc. 2560.09, exp. 2560.04), which was consistent with the structural skeleton (Fig. S7 and Table S9†). These results indicate that both **Dy$_6$** and **HNP-Dy$_6$** exhibited high stabilities in solution (Fig. 3b and 4b). Based on the structural analysis results of **Dy$_6$** and **HNP-Dy$_6$**, their stabilities can be attributed to the two large-volume chelating ligands on the cluster core periphery tightly wrapping around the cluster core, effectively resisting
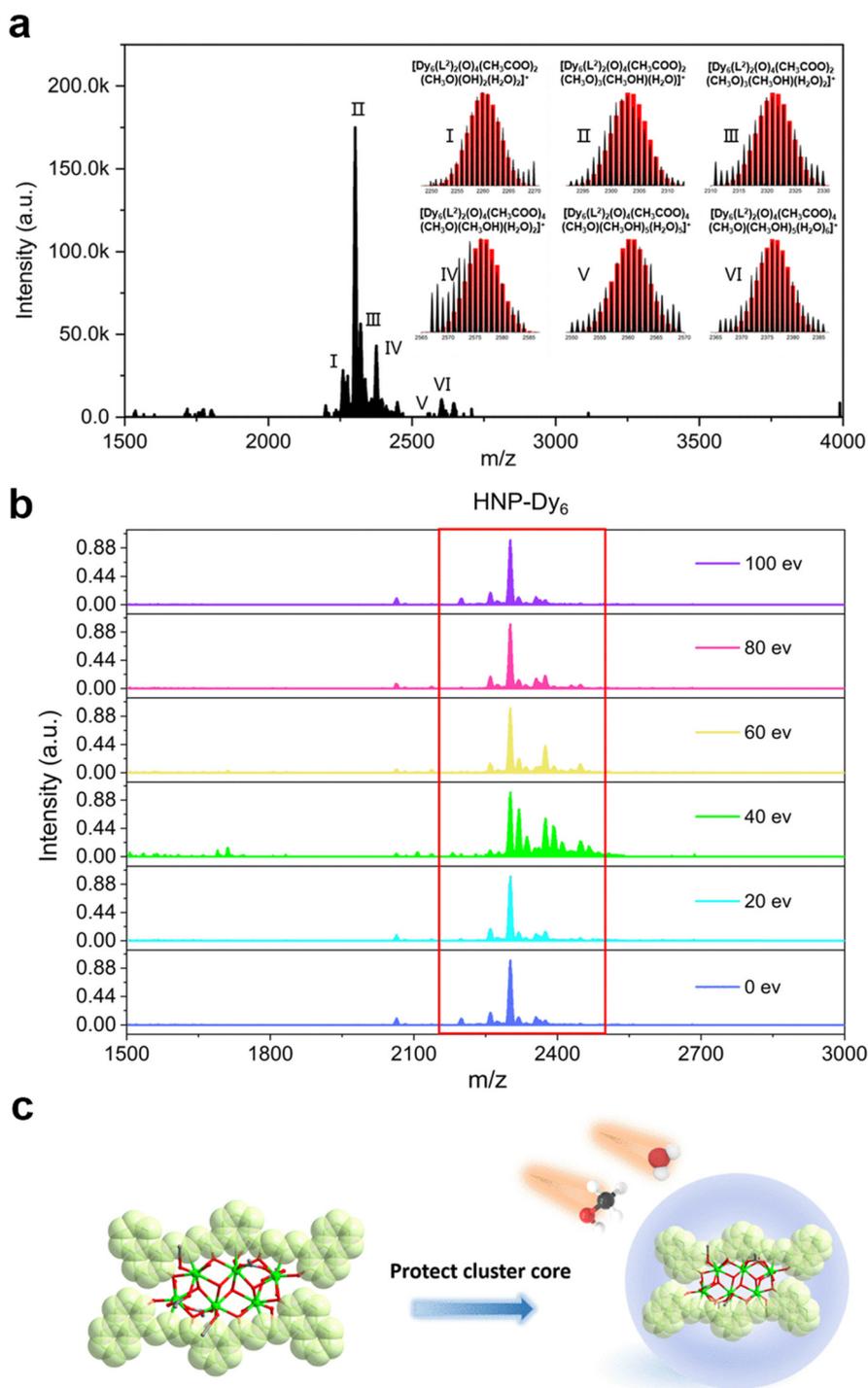
This journal is © the Partner Organisations 2023

Inorg. Chem. Front., 2023, **10**, 6269–6281 | **6273**
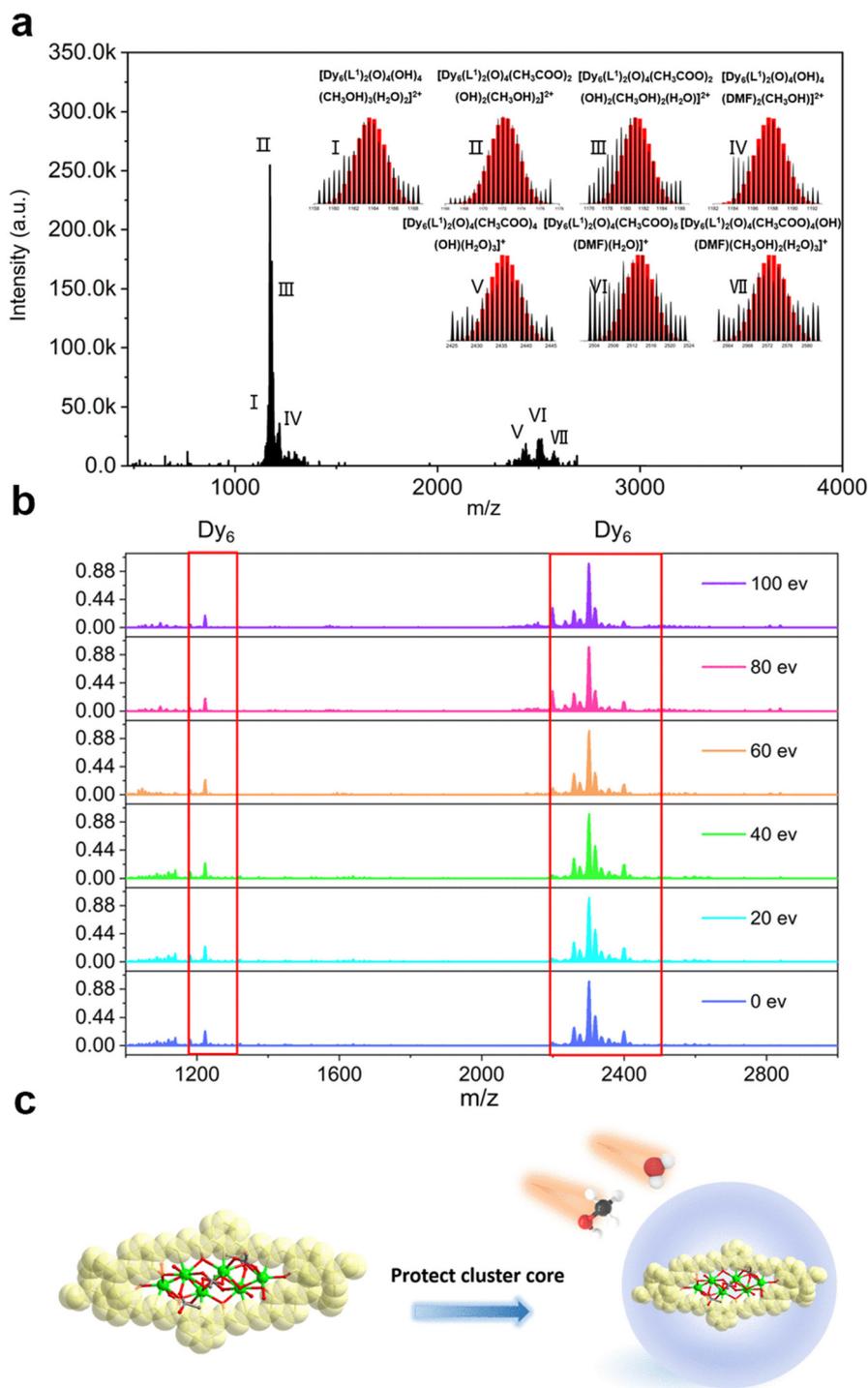
Fig. 3 (a) HRESI-MS spectrum of **Dy₆** dissolved in DMF in the positive-ion mode, (b) HRESI-MS spectrum of **Dy₆** dissolved in DMF under different ion-source voltages (in-source CID), and (c) schematic of the chelating ligands effectively protecting the cluster core.

the attack of foreign solvent molecules on the cluster core (Fig. 3c and 4c).

Assembly mechanism of Dy₆ and HNP-Dy₆

We further explored the self-assembly mechanism of **Dy₆** and **HNP-Dy₆** by performing time-dependent HRESI-MS to track

the species changes separately during their formation (Fig. 5a and 6a and Tables S10 and S11†). The HRESI-MS data suggested that **Dy₆** was formed through a step-by-step assembly. Fig. 5b depicts the time-dependent change trend of the species in the solution during the self-assembly process of **Dy₆**. First, the reaction system was stirred at room temperature

6274 | *Inorg. Chem. Front.*, 2023, **10**, 6269–6281

This journal is © the Partner Organisations 2023

Fig. 4 (a) HRESI-MS spectrum of **HNP-Dy$_6$** dissolved in DMF in the positive-ion mode, (b) HRESI-MS spectrum of **HNP-Dy$_6$** dissolved in DMF under different ion-source voltages (in-source CID), and (c) schematic of the chelating ligands effectively protecting the cluster core.

for 5 min (0 min), during which the ligand H$_2$L immediately reacted with the metal Dy(III) ions to generate multiple [Dy$_2$L^1] fragments. The ligand fragment with the highest intensity appeared in the m/z = 877.49 position, which can be assigned to [Dy$_2$(L^1)(OH)$_2$(DMF)$_8$(CH$_3$OH)$_6$(H$_2$O)$_4$]$^{2+}$ (Fig. 5a and S8†). The other molecular-ion peak fragments related to [Dy$_2$L^1]

appeared at positions m/z = 878.48 and 891.50. By fitting, the molecular formulas of these fragments were found as [Dy$_2$(L^1)(OH)$_2$(DMF)$_8$(CH$_3$OH)$_5$(H$_2$O)$_6$]$^{2+}$ (calc. 878.37, exp. 878.48) and [Dy$_2$(L^1)(OH)$_2$(DMF)$_8$(CH$_3$OH)$_8$(H$_2$O)$_2$]$^{2+}$ (calc. 891.40, exp. 891.50) (Fig. 5a and S8†). The experimental results showed that the H$_2$L^1 ligand removed two protons and pre-

This journal is © the Partner Organisations 2023
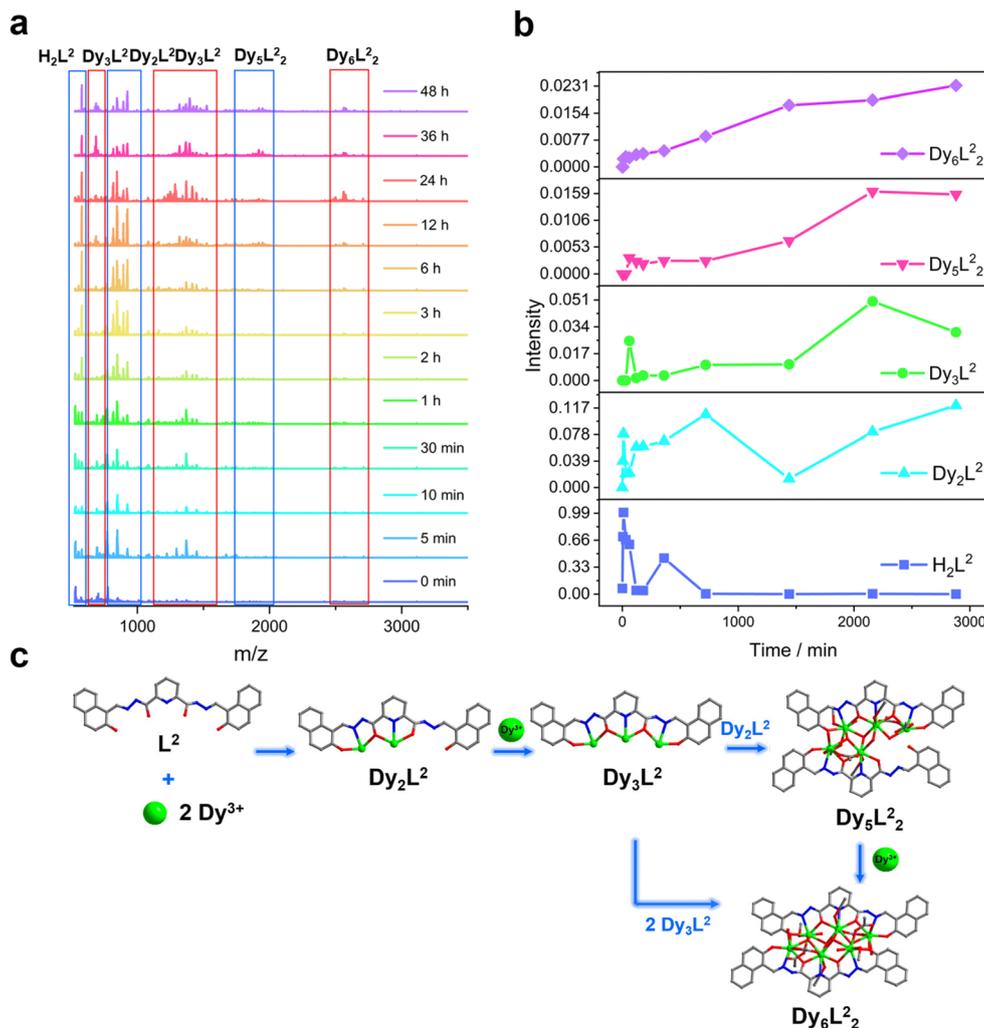
Inorg. Chem. Front., 2023, **10**, 6269–6281 | **6275**
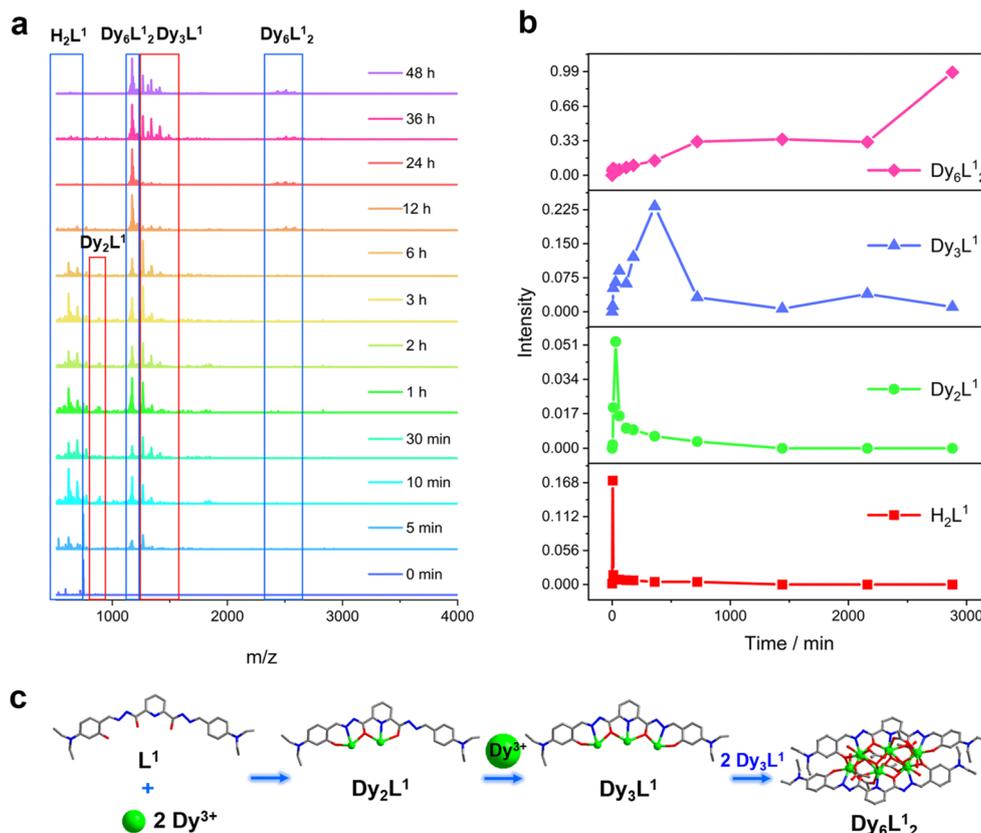
Fig. 5 (a) Time-dependent HRESI-MS tracking of the **Dy$_6$** formation process, (b) intensity–time curves of the molecular-ion peaks of different species during the reaction, and (c) schematic of the possible formation process and the self-assembly mechanism of **Dy$_6$**.

sented −2 valence under triethylamine regulation, while the $(L^1)^{2-}$ ligand removed two protons combined with two metal-centered Dy(III) ions to form the $[Dy_2L^1]$ fragments. The intensity of the $[Dy_2L^1]$ fragments gradually decreased with increasing reaction time. These fragments disappeared after heating for 12 h and were transformed into a small amount of $[Dy_3L^1]$ fragments with the increasing heating time. They began to appear at 5 min, formed in large quantities at 1 h, reached the maximum intensity at 6 h, and weakened after 12 h. Their molecular-ion peak appeared in the $m/z = 1242.03$–1416.14 range, and the molecular formulas obtained by fitting were $[Dy_3(L^1)(OH)_6(DMF)(H_2O)_2]^+$ (calc. 1242.13, exp. 1242.03), $[Dy_3(L^1)(OH)_6(CH_3OH)_2(H_2O)_2]^+$ (calc. 1265.16, exp. 1265.08), $[Dy_3(L^1)(OH)_6(DMF)_2(CH_3OH)_2]^+$ (calc. 1345.07, exp. 1345.23), and $[Dy_3(L^1)(OH)_6(DMF)_2(CH_3OH)_2(H_2O)_4]^+$ (calc. 1416.26, exp. 1416.14) (Fig. 5a and S8†). The $[Dy_6L^1_2]$ fragments also began to appear at 5 min from the beginning of the reaction, formed in large quantities at 6 h, and showed a gradually increasing intensity. The molecular-ion peaks related to $[Dy_6L^1_2]$ were observed in the $m/z = 1151.53$–2572.22 range. The molecular formulas of these fragments obtained by fitting were $[Dy_6(L^1)_2(O)_4(CH_3COO)(OH)_3(CH_3OH)_2]^{2+}$ (calc. 1151.58, exp. 1151.53), $[Dy_6(L^1)_2(O)_4(OH)_4(CH_3OH)_3(H_2O)_2]^{2+}$ (calc. 1163.59, exp. 1163.54), $[Dy_6(L^1)_2(O)_4(CH_3COO)_2(OH)_2(CH_3OH)_2]^{2+}$ (calc. 1172.58, exp. 1172.55), $[Dy_6(L^1)_2(O)_4$

$(CH_3COO)_2(OH)_2(CH_3OH)_2(H_2O)]^{2+}$ (calc. 1181.09, exp. 1181.08), $[Dy_6(L^1)_2(O)_4(OH)_4(DMF)_2(CH_3OH)]^{2+}$ (calc. 1188.10, exp. 1188.08), $[Dy_6(L^1)_2(O)_4(CH_3COO)_5(DMF)]^+$ (calc. 2496.21, exp. 2496.20), $[Dy_6(L^1)_2(O)_4(CH_3COO)_5(DMF)(H_2O)]^+$ (calc. 2513.20, exp. 2513.18), and $[Dy_6(L^1)_2(O)_4(CH_3COO)_4(OH)(DMF)(CH_3OH)_2(H_2O)_3]^+$ (calc. 2572.26, exp. 2572.22) (Fig. 5a and S8). Surprisingly, the $[Dy_6L^1_2]$ fragments also began appearing at the same time as the $[Dy_3L^1]$ fragments were detected at 5 min from the start of the reaction. The results indicate that the trinuclear fragment $[Dy_3L^1]$ was quickly used as a template motif after its formation to rapidly react to form the $[Dy_6L^1_2]$ fragment. Therefore, the formation process of **Dy$_6$** underwent a stepwise assembly and had the possible assembly mechanism of $L^1 + 2Dy \rightarrow Dy_2L^1 \rightarrow Dy_3L^1 \rightarrow 2Dy_3L^1 \rightarrow Dy_6L^1_2$ (Fig. 5c).

Similarly, we tracked the **HNP-Dy$_6$** formation using time-dependent HRESI-MS and proposed its possible self-assembly mechanism. First, the reaction system was stirred at room temperature for 5 min (the label in the figure is 0 min), during which the ligand H_2L immediately reacted with the metal-centered Dy(III) ions to generate multiple $[Dy_2L^2]$ fragments. The ligand fragment with the highest intensity appeared in the $m/z = 925.03$ position that can be assigned to $[Dy_2(L^2)(CH_3O)_2(OH)(H_2O)]^+$ (Fig. 6a and S9†). The other molecular-ion peak fragments related to $[Dy_2L^2]$ appeared at positions 1008.93 and 1070.96. The molecular formulas of these fragments obtained

6276 | *Inorg. Chem. Front.*, 2023, **10**, 6269–6281

This journal is © the Partner Organisations 2023

Fig. 6 (a) Time-dependent HRESI-MS tracking of the **HNP-Dy₆** formation process, (b) HRESI-MS spectra intensity–time profiles of the species, and (c) schematic of the possible assembly mechanism of **HNP-Dy₆**.

by fitting were $[Dy_2(L^2)(CH_3O)_2(OH)(CH_3OH)(H_2O)_4]^+$ (calc. 1009.10, exp. 1008.93) and $[Dy_2(L^2)(OH)_3(DMF)_2(CH_3OH)(H_2O)]^+$ (calc. 1071.14, exp. 1070.96). We also observed that a small amount of $[Dy_2L^2]$ fragments chelated with the metal-centered Dy(III) ions to form the $[Dy_3L^2]$ fragments, which began appearing at 5 min. Their molecular-ion peaks appeared at the m/z = 1342.08–1524.10 position. The molecular formulas of these fragments obtained by fitting were $[Dy_3(L^2)(OH)_6(DMF)_3(CH_3OH)]^+$ (calc. 1342.13, exp. 1342.08), $[Dy_3(L^2)(OH)_6(DMF)(CH_3OH)_3(H_2O)_6]^+$ (calc. 1370.16, exp. 1370.07), $[Dy_3(L^2)(OH)_6(DMF)(CH_3OH)_4(H_2O)_2]^+$ (calc. 1448.22, exp. 1448.08), and $[Dy_3(L^2)(OH)_6(DMF)_2(CH_3OH)_5(H_2O)_7]^+$ (calc. 1524.26, exp. 1524.10) (Fig. 6a and S9†). With the continuous increase of the heating time, the $[Dy_5L^2_2]$ fragments started to appear at 1 h and formed by chelating a $[Dy_2L^2]$ fragment with a $[Dy_3L^2]$ fragment. The molecular-ion peak of the $[Dy_5L^2_2]$ fragment was observed at the m/z = 1919.98–1967.96 position. The molecular formulas of these fragments acquired by fitting were $[Dy_5(L^2)_2(O)_4(OH)_2]^+$ (calc. 1919.95,

exp. 1919.98), $[Dy_5(L^2)_2(O)_4(OH)_2(CH_3OH)]^+$ (calc. 1946.94, exp. 1946.96), and $[Dy_5(L^2)_2(O)_4(OH)_2(CH_3OH)(H_2O)]^+$ (calc. 1967.98, exp. 1967.96). The $[Dy_3L^2]$ and $[Dy_5L^2_2]$ fragments gradually disappeared with up 48 h of heating time. The $[Dy_6L^2_2]$ fragments also began to appear at 5 min from the beginning of the reaction, formed in large quantities at 6 h, and showed a gradually increasing intensity. The molecular-ion peaks related to the $[Dy_6L^2_2]$ fragments appeared in the m/z = 2261.87–2576.04 range. The molecular formulas of these fragments obtained by fitting were $[Dy_6(L^2)_2(O)_4(CH_3COO)_2(CH_3O)(OH)_2(H_2O)_2]^+$ (calc. 2261.91, exp. 2261.87), $[Dy_6(L^2)_2(O)_4(CH_3COO)_2(CH_3O)_3(CH_3OH)(H_2O)]^+$ (calc. 2302.96, exp. 2302.87), $[Dy_6(L^2)_2(O)_4(CH_3COO)_2(CH_3O)_3(CH_3OH)(H_2O)_2]^+$ (calc. 2321.97, exp. 2321.89), $[Dy_6(L^2)_2(O)_4(CH_3COO)_4(CH_3O)(CH_3OH)(H_2O)_2]^+$ (calc. 2375.96, exp. 2375.94), $[Dy_6(L^2)_2(O)_4(CH_3COO)_4(CH_3O)(CH_3OH)_5(H_2O)_5]^+$ (calc. 2560.09, exp. 2560.04), and $[Dy_6(L^2)_2(O)_4(CH_3COO)_4(CH_3O)(CH_3OH)_5(H_2O)_6]^+$ (calc. 2576.10, exp. 2576.04) (Fig. 6a and S9†). Therefore, the formation process of **HNP-Dy₆** was a combination of the stepwise

This journal is © the Partner Organisations 2023

Inorg. Chem. Front., 2023, **10**, 6269–6281 | **6277**

and template assemblies with two possible self-assembly mechanisms: $L^2 + 2Dy \rightarrow Dy_2L^2 \rightarrow Dy_3L^2 \rightarrow Dy_5L^2_2 \rightarrow Dy_6L^2_2$ or $L^2 + 2Dy \rightarrow Dy_2L^2 \rightarrow Dy_3L^2 \rightarrow 2Dy_3L^2 \rightarrow Dy_6L^2_2$ (Fig. 6c).

MRI performance of Gd$_6$

As one of the most mature medical imaging techniques available, MRI has been extensively used in clinical medical diagnosis in the recent years. However, CAs are usually required to improve the imaging contrast and clarity of MRI.[12,13,35–38] Therefore, CAs with high resolution and clear imaging effects must be designed and developed. Gadolinium-based chelates are currently extensively used as a T_1-weighted MRI CA for clinical diagnosis, and they usually require higher doses to achieve excellent imaging results.[39–41] To explore the feasibility of **Gd$_6$** as a T_1-weighted MRI CA, we tested the relaxation time with the Gd(III) concentration changes at 1-T magnetic field strength and obtained the longitudinal and transverse relaxation rates (r_1 and r_2, respectively). The results showed the **Gd$_6$** r_1 and r_2 values of 12.06 and 24.10 mM^{-1} s^{-1}, respectively, at 1-T magnetic field strength (Fig. 7a). **Gd$_6$** with a highly aggregated Gd(III) exhibited higher relaxation rates compared to the conventional Gd chelates. $r_2/r_1 = 1.99$ ($r_2/r_1 < 2$) indicated that **Gd$_6$** is a potential T_1-weighted MRI CA candidate.[12,42,43] Under the same magnetic field, the r_1 and r_2 of gadopentetate dimeglumine injection (Gd-DTPA), a currently used clinical MRI contrast agent, are 4.55 and 5.77 mM^{-1} s^{-1}, respectively.[12] In comparison, **Gd$_6$** shows higher relaxation values. With the gradual increase of the Gd(III) concentration of **Gd$_6$** in the aqueous solution, the T_1-weighted image gradually became brighter under 1-T magnetic field. By contrast, the T_2-weighted image gradually turned darker from bright, indicating that **Gd$_6$** exhibited a good T_1 imaging effect in the solution. The T_1 mapping images displayed by different **Gd$_6$** concentrations at 1-T magnetic field also depicted its great potential as an MRI CA in biomedical diagnosis (Fig. 7b). In addition, we dissolved **Gd$_6$** crystals in DMSO and dispersed them in H$_2$O and phosphate buffered saline (PBS), respectively, and recorded the **Gd$_6$**

dispersed in the above solutions in 1–5 days by UV-visible absorption spectroscopy, which was the absorbance (OD) change at 422 nm. We found that there was no significant change in the absorbance of **Gd$_6$** at 422 nm from the 1–5 days. The results show that **Gd$_6$** has excellent stability (Fig. S10†).[5,12]

Magnetic analysis of Ln$_6$

Lanthanide complexes have been extensively explored as candidate materials for single-molecule magnets (SMMs) and magnetic refrigerants. Especially the dysprosium complexes constructed by Dy(III) ions are mainly attributed to their significant magnetic anisotropy.[34] Therefore, we investigated the magnetic behavior of **Dy$_6$** and **HNP-Dy$_6$**. The temperature-varying molar susceptibilities of the **Dy$_6$** and **HNP-Dy$_6$** pure phases were tested under an external DC magnetic field of 1000 Oe in the 2–300 K temperature range (Fig. S11a and 11c†).[44–49] The $\chi_m T$ values of **Dy$_6$** and **HNP-Dy$_6$** at 300 K were 83.65 and 82.13 cm^3 K mol^{-1}, respectively ($^6H_{15/2}$, $S = 5/2$, $g = 4/3$, $J = 15/2$, and $L = 5$). The $\chi_m T$ values of both **Dy$_6$** and **HNP-Dy$_6$** were slightly lower than the theoretical value (i.e., 85.02 cm^3 K mol^{-1}) of the six Dy(III) ions. As the temperature decreased, the $\chi_m T$ value of **Dy$_6$** continued to decrease, and when the temperature reached 2 K, the $\chi_m T$ of **Dy$_6$** dropped rapidly to 68.15 cm^3 K mol^{-1}. However, when the temperature decreased from 300 K to 2 K, the $\chi_m T$ value of **HNP-Dy$_6$** first increased slowly and then decreased, and its $\chi_m T$ value reached 82.13 cm^3 K mol^{-1} at 100 K, while its $\chi_m T$ decreased rapidly to 63.18 cm^3 K mol^{-1} when the temperature reached 2 K.[49,50] These findings showed that the temperature-decreasing $\chi_m T$ value may be caused by a decrease in the Stark sublevel of the Dy(III) excited state and the induced crystal field effect. Subsequently, we tested the field-dependent magnetization of **Dy$_6$** and **HNP-Dy$_6$** at different temperatures (2–5 K) and applied fields of 0–7 T. The M vs. H/T curves were plotted in Fig. S11b and 11d.† Their measured magnetizations at 2 K rapidly increased in the low-field region, but gradually became flat in the high-field region. **Dy$_6$** reached a maximum value of 75.98$N\beta$, while **HNP-Dy$_6$**
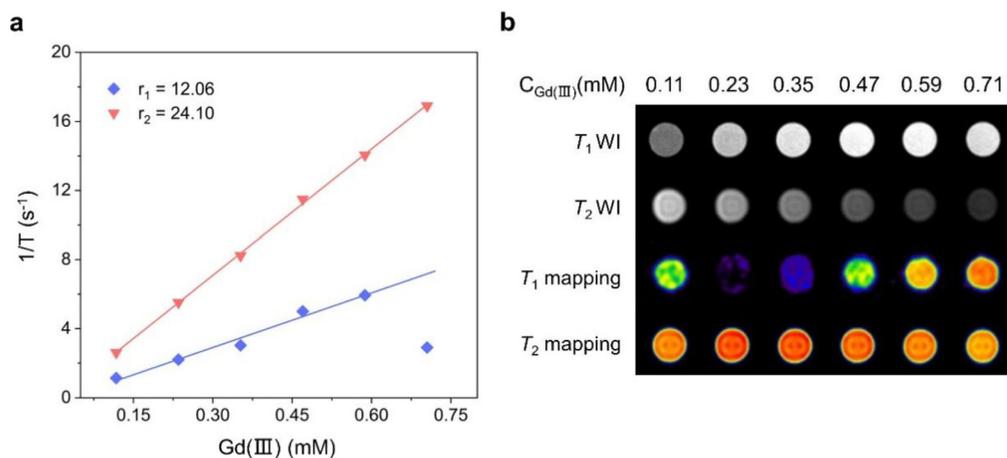

Fig. 7 (a) Comparison of the r_1 and r_2 of **Gd$_6$** under 1-T magnetic field and (b) comparison of the solution imaging of different **Gd$_6$** concentrations under 1-T magnetic field.

6278 | Inorg. Chem. Front., 2023, **10**, 6269–6281

This journal is © the Partner Organisations 2023

reached $36.90N\beta$ at a 13 kOe static field. The M *vs.* H/T curves of **Dy$_6$** and **HNP-Dy$_6$** at different temperatures did not significantly overlap. The test results indicated that the Dy(III) ions may have low excited states and/or a large magnetic anisotropy. The hysteresis loops of **Dy$_6$** and **HNP-Dy$_6$** in Fig. S12† were not obvious at 2 K, which may be due to the existence of the crystal field and strong quantum tunneling effects. We further tested the alternating-current susceptibility of **Dy$_6$** and **HNP-Dy$_6$** to explore their dynamic magnetic behavior. We found that neither of the **Dy$_6$** nor **HNP-Dy$_6$** out-of-phase (χ'') signals showed an obvious frequency-dependent behavior under the zero DC field (Fig. S13†). Generally speaking, multinuclear gadolinium clusters have better MCE properties and can be used as an excellent magnetocaloric material.[51,52] We tested the magnetocaloric effect of **Gd$_6$** at 2–8 K and 0–7 T. As shown in Fig. S14,† when T = 2 K and ΔH = 7 T, the maximum experimental entropy change value of **Gd$_6$** is 25.76 J kg^{-1} K^{-1}, which is smaller than the theoretical $-\Delta S_m$ value (40.06 J kg^{-1} K^{-1}), calculated based on the formula: $-\Delta S_m = nR \ln(2S + 1)$ (R = 8.3145 J mol^{-1} K^{-1}, S = 7/2). This can be attributed to the antiferromagnetic interaction between Gd(III) ions.[17] In addition, its $-\Delta S_m$ value is higher than most of the reported hexanuclear gadolinium clusters, showing better MCE performance.[26,51] Therefore, magnetic studies show that **Gd$_6$** is a potential magnetic refrigeration material.

Conclusions

In conclusion, diacylhydrazone-derived ligands are used to enable controllable construction of differentiated hexanuclear lanthanide clusters with identical cores but different template-motif arrangements. Different substituents are used to regulate the template-motif arrangements formed by multidentate chelating ligands, taking a big step toward the controllable and precise synthesis of lanthanide clusters. HRESI-MS results prove that the two hexanuclear lanthanide clusters obtained herein exhibit high stabilities in solutions. Time-dependent HRESI-MS is employed to track the formation of these hexanuclear lanthanide clusters and propose their possible formation mechanisms. The findings reveal a novel strategy for the rational construction of lanthanide clusters with specific shapes and template-motif arrangements. Notably, the aggregation of Gd(III) ions leads to considerably enhanced relaxation rates of the **Gd$_6$** clusters and an excellent MRI resolution. Magnetic studies show that **Gd$_6$** exhibits remarkable MCE performance, which can be used as a potential magnetic refrigeration material. This work presents a new idea for the controllable synthesis of complex clusters and promotes progress in the crystal engineering of clusters with precise structures.

Conflicts of interest

There are no conflicts to declare.

Acknowledgements

References

1 Z. Zhu, M. Guo, X. L. Li and J. Tang, Molecular magnetism of lanthanide: Advances and perspectives, *Coord. Chem. Rev.*, 2019, **378**, 350–364.

2 X. Z. Li, C. B. Tian and Q. F. Sun, Coordination-Directed Self-Assembly of Functional Polynuclear Lanthanide Supramolecular Architectures, *Chem. Rev.*, 2022, **122**, 6374–6458.

3 D. E. Barry, D. F. Caffrey and T. Gunnlaugsson, Lanthanide-directed synthesis of luminescent self-assembly supramolecular structures and mechanically bonded systems from acyclic coordinating organic ligands Dawn, *Chem. Soc. Rev.*, 2016, **45**, 3244–3274.

4 J. C. G. Bünzli, Lanthanide Luminescence for Biomedical Analyses and Imaging, *Chem. Rev.*, 2010, **110**, 2729–2755.

5 H. L. Wang, Z. Ni, Z. Y. Ruan, Z. H. Zhu, P. Y. Liao, G. Feng, J. H. Jia and M. L. Tong, Spherical lanthanide nanoclusters toward white-light emission and cell membrane imaging, *Nano Res.*, 2023, **16**, 11495–11502.

6 M. Liu, H. Li, L. Bai, K. Zheng, Z. Zhao, Z. Chen, S. W. Ng, L. Ding and C. Zeng, Real-time and visual sensing devices based on pH-control assembled lanthanide-barium nanocluster, *J. Hazard. Mater.*, 2021, **413**, 125291.

7 Y. Jiang, K. Zheng, Z. Liu, X. Yu, Q. Yang, T. Tang and C. Zeng, Synthesis of Two New Dinuclear Lanthanide Clusters and Visual Bifunctional Sensing Devices Based on the Eu Cluster, *Adv. Opt. Mater.*, 2022, **10**, 2102267.

8 D. Shao, W. J. Tang, Z. Ruan, X. Yang, L. Shi, X. Q. Wei, Z. Tian, K. Kumari and S. K. Singh, Water-driven reversible switching of single-ion magnetism and proton conduction in a dysprosium sulfonate, *Inorg. Chem. Front.*, 2022, **9**, 6147–6157.

9 D. Shao, P. P. Sahu, W. J. Tang, Y. L. Zhang, Y. Zhou, F. X. Xu, X. Q. Wei, Z. Tian, S. K. Singh and X. Y. Wang, A single-ion magnet building block strategy toward Dy$_2$ single-molecule magnets with enhanced magnetic performance, *Dalton Trans.*, 2022, **51**, 18610–18621.

10 N. Qiao, X. Y. Xin, X. F. Guan, C. X. Zhang and W. M. Wang, Self-Assembly Bifunctional Tetranuclear Ln$_2$Ni$_2$ Clusters: Magnetic Behaviors and Highly Efficient Conversion of CO$_2$ under Mild Conditions, *Inorg. Chem.*, 2022, **61**, 15098–15107.

11 X. L. Li, L. Zhao, J. Wu, W. Shi, N. Struch, A. Lützen, A. K. Powell, P. Cheng and J. Tang, Subcomponent self-assembly of circular helical Dy$_6$(L)$_6$ and bipyramid Dy$_{12}$(L)$_8$

This journal is © the Partner Organisations 2023

Inorg. Chem. Front., 2023, **10**, 6269–6281 | **6279**

architectures directed via second-order template effects, *Chem. Sci.*, 2022, **13**, 10048–10056.

12 H. L. Wang, D. L. Liu, J. H. Jia, J. L. Liu, Z. Y. Ruan, W. Deng, S. P. Yang, S. G. Wu and M. L. Tong, High-Stability Spherical Lanthanide Nanoclusters for Magnetic Resonance Imaging, *Natl. Sci. Rev.*, 2023, **10**, nwad036.

13 Z. Wang, L. He, B. Liu, L. P. Zhou, L. X. Cai, S. J. Hu, X. Z. Li, Z. Li, T. Chen, X. Li and Q. F. Sun, Coordination-Assembled Water-Soluble Anionic Lanthanide Organic Polyhedra for Luminescent Labeling and Magnetic Resonance Imaging, *J. Am. Chem. Soc.*, 2020, **142**, 16409–16419.

14 Y. L. Li, H. L. Wang, Z. H. Zhu, F. P. Liang and H. H. Zou, Recent advances in the structural design and regulation of lanthanide clusters: Formation and self-assembly mechanisms, *Coord. Chem. Rev.*, 2023, **493**, 215322.

15 X. Y. Zheng, J. Xie, X. J. Kong, L. S. Long and L. S. Zheng, Recent advances in the assembly of high-nuclearity lanthanide clusters, *Coord. Chem. Rev.*, 2019, **378**, 222–236.

16 X. Y. Zheng, Y. H. Jiang, G. L. Zhuang, D. P. Liu, H. G. Liao, X. J. Kong, L. S. Long and L. S. Zheng, A Gigantic Molecular Wheel of $\{Gd_{140}\}$: A New Member of the Molecular Wheel Family, *J. Am. Chem. Soc.*, 2017, **139**, 18178–18181.

17 X. M. Luo, Z. B. Hu, Q. F. Lin, W. Cheng, J. P. Cao, C. H. Cui, H. Mei, Y. Song and Y. Xu, Exploring the Performance Improvement of Magnetocaloric Effect Based Gd-Exclusive Cluster Gd_{60}, *J. Am. Chem. Soc.*, 2018, **140**, 11219–11222.

18 X. Y. Li, H. F. Su, Q. W. Li, R. Feng, H. Y. Bai, H. Y. Chen, J. Xu and X. H. Bu, A Giant Dy_{76} Cluster: A Fused Bi-Nanopillar Structural Model for Lanthanide Clusters, *Angew. Chem., Int. Ed.*, 2019, **58**, 10184–10188.

19 L. Qin, Y. Z. Yu, P. Q. Liao, W. Xue, Z. Zheng, X. M. Chen and Y. Z. Zheng, A "Molecular Water Pipe": A Giant Tubular Cluster $\{Dy_{72}\}$ Exhibits Fast Proton Transport and Slow Magnetic Relaxation, *Adv. Mater.*, 2016, **28**, 10772–10779.

20 W. Huang, W. Chen, Q. Bai, Z. Zhang, M. Feng and Z. Zheng, Anion-Guided Stepwise Assembly of High-Nuclearity Lanthanide Hydroxide Clusters, *Angew. Chem., Int. Ed.*, 2022, **61**, e2022053.

21 Z. H. Zhu, X. F. Ma, H. L. Wang, H. H. Zou, K. Q. Mo, Y. Q. Zhang, Q. Z. Yang, B. Li and F. P. Liang, A triangular Dy_3 single-molecule toroic with high inversion energy barrier: magnetic properties and multiple-step assembly mechanism, *Inorg. Chem. Front.*, 2018, **5**, 3155–3162.

22 H. L. Wang, X. F. Ma, J. M. Peng, Z. H. Zhu, B. Li, H. H. Zou and F. P. Liang, Tracking the Stepwise Formation of the Dysprosium Cluster (Dy_{10}) with Multiple Relaxation Behavior, *Inorg. Chem.*, 2019, **58**, 9169–9174.

23 Z. H. Zhu, J. M. Peng, H. L. Wang, H. H. Zou and F. P. Liang, Assembly Mechanism and Heavy Metal Ion Sensing of Cage-Shaped Lanthanide Nanoclusters, *Cell Rep. Phys. Sci.*, 2020, **1**, 100165.

24 H. L. Wang, T. Liu, Z. H. Zhu, J. M. Peng, H. H. Zou and F. P. Liang, A series of dysprosium clusters assembled by a substitution effect-driven out-to-in growth mechanism, *Inorg. Chem. Front.*, 2021, **8**, 2136–2143.

25 Y. L. Li, H. L. Wang, Z. H. Zhu, J. Li, H. H. Zou, J. M. Peng and F. P. Liang, Truncation reaction regulates the out-to-in growth mechanism to decrypt the formation of brucite-like dysprosium clusters, *Dalton Trans.*, 2022, **51**, 197–202.

26 Y. L. Li, H. L. Wang, Z. H. Zhu, J. Li, H. H. Zou and F. P. Liang, A Series of High-Nuclear Gadolinium Cluster Aggregates with a Magnetocaloric Effect Constructed through Two-Component Manipulation, *Inorg. Chem.*, 2021, **60**, 16794–16802.

27 B. F. Long, S. Yu, Z. H. Zhu, Y. L. Li, F. F. Liang and H. H. Zou, Coordination site manipulation of the annular growth mechanism to assemble chiral lanthanide clusters with different shapes and magnetic properties, *Inorg. Chem. Front.*, 2022, **9**, 5950–5959.

28 B. F. Long, Y. L. Li, Z. H. Zhu, H. L. Wang, F. P. Liang and H. H. Zou, Assembly of pinwheel/twist-shaped chiral lanthanide clusters with rotor structures by an annular/linear growth mechanism and their magnetic properties, *Dalton Trans.*, 2022, **416**, 17040–17049.

29 Z. R. Luo, H. L. Wang, Z. H. Zhu, T. Liu, X. F. Ma, H. F. Wang, H. H. Zou and F. P. Liang, Assembly of Dy_{60} and Dy_{30} cage-shaped nanoclusters, *Commun. Chem.*, 2020, **3**, 1–9.

30 H. L. Wang, T. Liu, Z. H. Zhu, J. M. Peng, H. H. Zou and F. P. Liang, A series of dysprosium clusters assembled by a substitution effect-driven out-to-in growth mechanism, *Inorg. Chem. Front.*, 2021, **8**, 2136–2143.

31 J. M. Peng, H. L. Wang, Z. H. Zhu, J. Bai, F. P. Liang and H. H. Zou, Series of the Largest Dish-Shaped Dysprosium Nanoclusters Formed by In Situ Reactions, *Inorg. Chem.*, 2022, **61**, 6094–6100.

32 H. L. Wang, Y. L. Li, Z. H. Zhu, X. L. Lu, F. P. Liang and H. H. Zou, Anion-Manipulated Hydrolysis Process Assembles of Giant High-Nucleation Lanthanide-Oxo Cluster, *Inorg. Chem.*, 2022, **61**, 20169–20176.

33 H. L. Wang, T. Liu, Z. H. Zhu, J. M. Peng, H. H. Zou and F. P. Liang, pH manipulates the assembly of a series of dysprosium clusters with subtle differences, *Inorg. Chem. Front.*, 2021, **8**, 3134–3140.

34 Y. L. Li, W. W. Qin, L. H. L. Wang, Z. Z. Zhu, F. P. Liang and H. H. Zou, Highly Stable Drone-shaped Lanthanide Clusters: Structure, Assembly Mechanism, and Crystalline-Amorphous Transitions, *Inorg. Chem. Front.*, 2023, **10**, 5337–5346.

35 J. Wahsner, E. M. Gale, A. Rodríguez-Rodríguez and P. Caravan, Chemistry of MRI Contrast Agents: Current Challenges and New Frontiers, *Chem. Rev.*, 2019, **119**, 957–1057.

36 D. Ni, W. Bu, E. B. Ehlerding, W. Cai and J. Shi, Engineering of inorganic nanoparticles as magnetic resonance imaging contrast agents, *Chem. Soc. Rev.*, 2017, **46**, 7438–7468.

6280 | *Inorg. Chem. Front.*, 2023, **10**, 6269–6281

This journal is © the Partner Organisations 2023

37 E. Debroye and T. N. Parac-Vogt, Towards polymetallic lanthanide complexes as dual contrast agents for magnetic resonance and optical imaging, *Chem. Soc. Rev.*, 2014, **43**, 8178–8192.

38 H. Li and T. J. Meade, Molecular Magnetic Resonance Imaging with Gd(III)-Based Contrast Agents: Challenges and Key Advances, *J. Am. Chem. Soc.*, 2019, **141**, 17025–17041.

39 P. Verwilst, S. Park, B. Yoon and J. S. Kim, Recent advances in Gd-chelate based bimodal optical/MRI contrast agents, *Chem. Soc. Rev.*, 2015, **44**, 1791–1806.

40 C. Sun, H. Lin, X. Gong, Z. Yang, Y. Mo, X. Chen and J. Gao, DOTA-Branched Organic Frameworks as Giant and Potent Metal Chelators, *J. Am. Chem. Soc.*, 2020, **142**, 198–206.

41 P. Caravan, J. J. Ellison, T. J. McMurry and R. B. Lauffer, Gadolinium(III) Chelates as MRI Contrast Agents: Structure, Dynamics, and Applications, *Chem. Rev.*, 1999, **99**, 2293–2352.

42 C. He, X. Wu, J. Kong, T. Liu, X. Zhang and C. Duan, A hexanuclear gadolinium–organic octahedron as a sensitive MRI contrast agent for selectively imaging glucosamine in aqueous media, *Chem. Commun.*, 2012, **48**, 9290–9292.

43 R. Wang, L. An, J. He, M. Li, J. Jiao and S. Yang, A class of water-soluble Fe(III) coordination complexes as T_1-weighted MRI contrast agents, *J. Mater. Chem. B*, 2021, **9**, 1787–1791.

44 J. Liu, Y. C. Chen, J. L. Liu, V. Vieru, L. Ungur, J. H. Jia, L. F. Chibotaru, Y. Lan, W. Wernsdorfer, S. Gao, X. M. Chen and M. L. Tong, A Stable Pentagonal Bipyramidal Dy(III) Single-Ion Magnet with a Record Magnetization Reversal Barrier over 1000 K, *J. Am. Chem. Soc.*, 2016, **138**, 5441–5450.

45 Z. Zhu, C. Zhao, T. Feng, X. Liu, X. Ying, X. L. Li, Y. Q. Zhang and J. Tang, Air-Stable Chiral Single-Molecule Magnets with Record Anisotropy Barrier Exceeding 1800 K, *J. Am. Chem. Soc.*, 2021, **143**, 10077–10082.

46 P. Zhang, L. Zhang, C. Wang, S. Xue, S. Y. Lin and J. Tang, Equatorially Coordinated Lanthanide Single Ion Magnets, *J. Am. Chem. Soc.*, 2014, **136**, 4484–4487.

47 B. Zhang, Z. Cheng, Y. Wu, L. Chen, R. Jing, X. Cai, C. Jiang, Y. Q. Zhang, A. Yuan, H. H. Cui and Z. Y. Li, Pseudo-mono-axial ligand fields that support high energy barriers in triangular dodecahedral Dy(III) single-ion magnets, *Chem. Sci.*, 2022, **13**, 13231–13240.

48 H. S. Wang, P. F. Zhou, J. Wang, Q. Q. Long, Z. Hu, Y. Chen, J. Li, Y. Song and Y. Q. Zhang, Significantly Enhancing the Single-Molecule-Magnet Performance of a Dinuclear Dy(III) Complex by Utilizing an Asymmetric Auxiliary Organic Ligand, *Inorg. Chem.*, 2021, **60**, 18739–18752.

49 J. L. Liu, Y. C. Chen and M. L. Tong, Symmetry strategies for high performance lanthanide-based single-molecule magnets, *Chem. Soc. Rev.*, 2018, **47**, 2431–2453.

50 Y. C. Chen, J. L. Liu, L. Ungur, J. Liu, Q. W. Li, L. F. Wang, Z. P. Ni, L. F. Chibotaru, X. M. Chen and M. L. Tong, Symmetry-Supported Magnetic Blocking at 20 K in Pentagonal Bipyramidal Dy(III) Single-Ion Magnets, *J. Am. Chem. Soc.*, 2016, **138**, 2829–2837.

51 J. Lu, V. Montigaud, O. Cador, J. Wu, L. Zhao, X. L. Li, M. Guo, B. Le Guennic and J. Tang, Lanthanide(III) Hexanuclear Circular Helicates: Slow Magnetic Relaxation, Toroidal Arrangement of Magnetic Moments, and Magnetocaloric Effect, *Inorg. Chem.*, 2019, **58**, 11903–11911.

52 Y. P. Qu, X. D. Huang, K. Xu, S. S. Bao and L. M. Zheng, Octahedral lanthanide clusters containing a central PO_4^{3-} anion: structural, luminescent, magnetic and relaxometric properties, *Dalton Trans.*, 2023, **52**, 10489–10498.

This journal is © the Partner Organisations 2023

Inorg. Chem. Front., 2023, **10**, 6269–6281 | **6281**